CRADA 0679
FINAL REPORT

Uncooled Micro-Cantilever Based Infrared Imager Optimization

1. Abstract

We report on the development, fabrication and characterization of microcantilever based uncooled focal plane array (FPA) for infrared imaging. By combining a streamlined design of microcantilever thermal transducers with a highly efficient optical readout, we minimized the fabrication complexity while achieving a competitive level of imaging performance. The microcantilever FPAs were fabricated using a straightforward fabrication process that involved only three photolithographic steps (i.e. three masks). A designed and constructed prototype of an IR imager employed a simple optical readout based on a noncoherent low-power light source. The main figures of merit of the IR imager were found to be comparable to those of uncooled MEMS infrared detectors with substantially higher degree of fabrication complexity. In particular, the *NETD* and the response time of the implemented MEMS IR detector were measured to be as low as 0.5K and 6 ms, respectively. The potential of the implemented designs can also be concluded from the fact that the constructed prototype enabled IR imaging of close to room temperature objects without the use of any advanced data processing. The most unique and practically valuable feature of the implemented FPAs, however, is their scalability to high resolution formats, such as 2000x2000, without progressively growing device complexity and cost.

2. Statement of Objectives

The overall technical objective of the proposed work was to develop uncooled infrared arrays based on micromechanical sensors. Currently used miniature sensors use a number of different readout techniques to accomplish the sensing. The use of optical readout techniques sensing require the deposition of thin coatings on the surface of micromechanical thermal detectors. Oak Ridge National Laboratory (ORNL) is uniquely qualified to perform the required research & development (R&D) services that will assist our ongoing activities. Over the past decade ORNL has developed a number of unique methods and techniques that led to improved sensors using a number of different approaches.

3. Benefits to the Funding DOE Office's Mission

The goal of this project was to develop microcantilever based uncooled focal plane array that will be able to respond to infrared radiation. The work involves the use of expertise and facilities present at ORNL. ORNL is uniquely qualified to perform the required research. Potential

applications of this work are uses in the characterization of chemical compounds of interest to DOE and national security applications.

4. Technical Discussion of Work Performed by All Parties

In recent years, there has been a growing interest in various MEMS based sensors for applications ranging from biomedicine to environmental monitoring, to thermal imaging. The scope of the present studies is related to unique advantages of focal plane arrays (FPAs) of thermal detectors based on the MEMS platform. Several research groups have already explored such FPAs and demonstrated their operation as uncooled infrared imaging devices [1-4]. It is worthy to note that fundamental models of MEMS FPAs predict that they can match or even exceed the performance of other, more conventional uncooled IR FPAs, such as those based on microbolometers [5-7]. In this paper, we report on the performance of an uncooled IR imager that incorporates a simplified MEMS FPA and a highly efficient low power optical readout.

The main goal of the present study is to demonstrate that, as compared to the previously implemented MEMS FPAs, further advantages can be taken from rationally designed MEMS thermal transducers, streamlined fabrication and a highly efficient optical readout. The most common MEMS readout means involve optical [4], capacitive [1], piezoresistive, and electron tunneling transduction principles [8]. Although all of these readout schemes can achieve extremely high sensitivity and acceptably low noise levels, only optical probing offers a contactless readout of MEMS sensing elements without the need for on-chip electronics and complex wiring architectures. The later requirement has largely limited the size of the microbolometer and other electronically probed FPAs to about 640×480 pixels. Furthermore, fabrication of FPAs integrated with the readout interconnects and electronics often involves complex high-cost processes, such as membrane transfer bonding.

4.1. Fabrication and Readout

The specific geometry of the pixels that we selected allowed us to arrange (tile) them into an array with a reasonably high fill factor. Figure 1 shows a fragment the 256 × 256 array of microcantilever IR detectors. The detectors are tiled in a pattern with a 75μm × 75μm pitch. Also shown in the insert is a close-up of a few pixels in which the patterning of the deposited Au layer is readily apparent. The darker area on the detector head is the bare SiN_x, and the brighter area on the detector head indicate the presence of Au. Two small rectangular openings in the center of the detector were designed to facilitate etching of the sacrificial oxide layer under the detector during the release step.

The diagram in Figure 2 illustrates the basic fabrication steps used in FPA fabrication. It is worthy to note that the process flow involved only three photolithographic steps. As a result, the overall level of fabrication complexity was significantly lower as compared to the fabrication of MEMS IR detectors reported previously. During the first photolithographic patterning, reactive ion etching was applied to the original double side polished Si wafers through a photoresist mask and resulted in formation of arrays of 5 μm tall posts necessary for anchoring the suspended

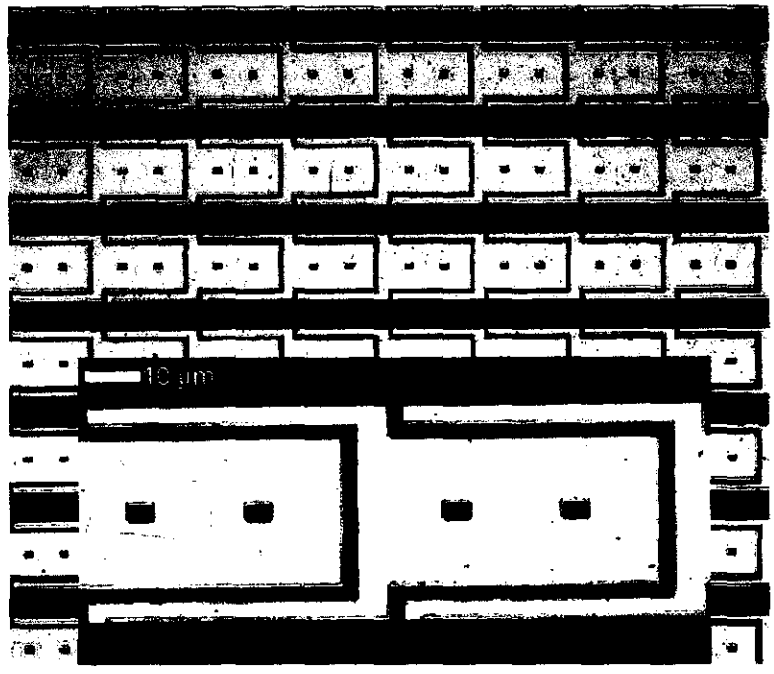

Fig. 1. Fragment of the fabricated 256 × 256 MEMS FPA. The selected geometry is characterized by a high fill factor and relaxed design rules.

structures. ICP SF_6 based etching process was used for Si etching. The next step involved conformal deposition of a 6.5 μm thick sacrificial layer on the Si surface with posts. Plasma enhanced chemical vapor deposition (PECVD) of silicon oxide at 250° C was used for this purpose. The sacrificial oxide layer was planarized using chemo-mechanical polishing (CMP) until a 4.5 μm thick oxide layer flush with the posts remained. This thickness of the sacrificial layer was chosen based on the requirement of an optimal IR resonant cavity to be formed between the Si substrate and the pixel structural layer. The CMP was followed by deposition of a 600 nm thick structural SiN_x layer on top of the planarized oxide surface. The second photolithography involved lift off patterning of a 120 nm Au layer evaporated on SiN_x. E-beam evaporation of the Au metallization was conducted immediately after depositing a 5 nm Cr adhesion layer. The pattern in the lift off photoresist layer corresponded to the superposition of the bimaterial leg sections and reflective regions of the pixel heads. This third photolithography was used to define the detector geometry in the SiN_x layer. The final steps of the FPA fabrications involved removal of the sacrificial layer using wet etching in the concentrated HF followed by rinsing and CO_2 critical point drying.

Schematic illustration of the implemented prototype of MEMS FPAs is shown in Figure 3. The IR radiation from the target was focused onto the array using a 50mm F=1 IR lens (TYTO, Janos Technology, Inc). The laser diode operated under a lasing threshold was used as a source of the probing light. The diverging light emitted by this spot source was re-focused by a 100 mm doublet lens so that it was converging to a size of the FPA at its plane. The total power of the beam and the power per pixel were approximately 1mW and a few nW, respectively. The beam reflected off the FPA reached its minimum cross-section at the front plane of the 30 mm lens

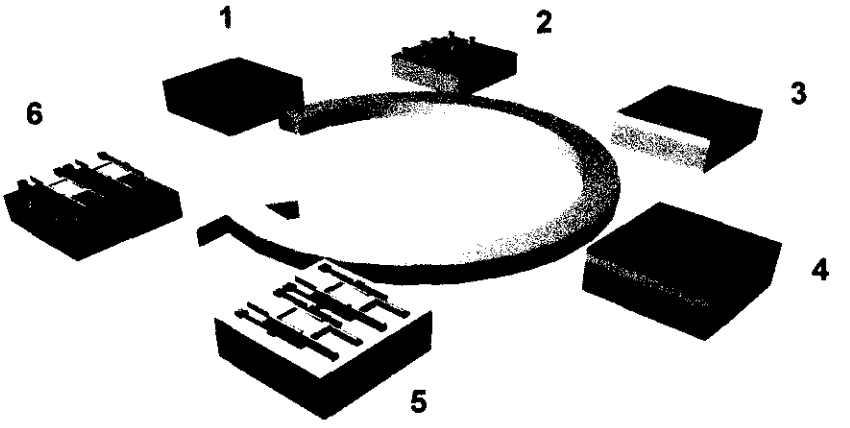

Fig. 3. 1) A double-polished Si wafer used as a substrate. 2) Fabrication process started with reactive ion etching that created posts on the silicon wafer. 3) SiO_2 sacrificial layer was deposited. 4) Chemo-mechanical polishing (CMP) was followed by deposition of a low-stress SiN_x layer. 5) Lift-off metallization was followed by patterning of the pixel geometry using RIE. 6) Wet etch of the sacrificial SiO_2 layer resulted in a released structure.

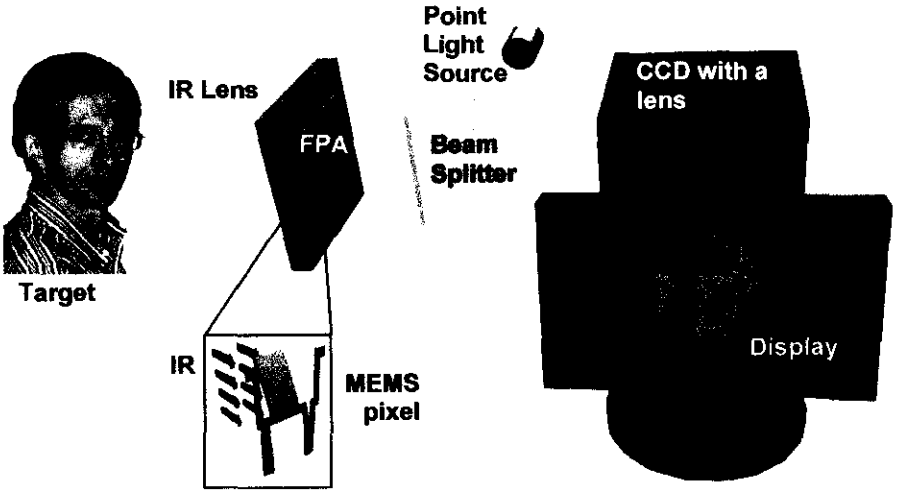

Fig. 2. Schematic illustration of the components and the arrangement used in the implemented prototype of a MEMS IR imager.

mounted on the CCD camera. The required angle-to-intensity conversion was achieved due to a small aperture (1/11) of this lens. Hence, the optical readout converted deflections of individual pixels (caused by different temperatures of the target being imaged) into proportionally varying intensities of the light projected onto a CCD chip. As a result, the object imaged by the MEMS FPA could be readily reconstructed by analyzing the output of a regular

12-bit CCD camera sensitive to visible light. Approximately one-to-one correspondence between the pixels of the CCD and those of the MEMS FPA was used in our experiments.

4.2. Results

In order to compare the performance of MEMS structures implemented in our present work to that of other detectors, we evaluated a series of figures of merit commonly used in the field [5,7], such as sensitivity, response time and noise equivalent temperature difference (*NETD*). According to the methodology established in our laboratory [6], experimental characterization started with measurements of the resonant frequency and thermal responsivity, $\Delta z/\Delta T$. The experimentally measured values of these parameters were compared against the computational predictions.

For the structures with a given geometry, finite element analysis predicts the first two resonant modes to be at 8.6 kHz and 14.5 kHz. The material properties used in these computations are displayed in Table 1. The two modes are attributable to the fundamental transverse resonance of the head and of the legs, respectively. In order to measure the resonant frequency, the structures were subject to optical excitation by the pump laser modulated with the lock-in reference signal and their response was measured as a function of excitation frequency. Typical response spectra for elements in the array are shown in Figure 4. The spectrum (curve "A") obtained using photothermal excitation [9] shows two resonances, at 7.4 kHz and 12 kHz. The spectrum obtained by spontaneous excitation due to ambient thermal energy (curve "B") shows similar resonance

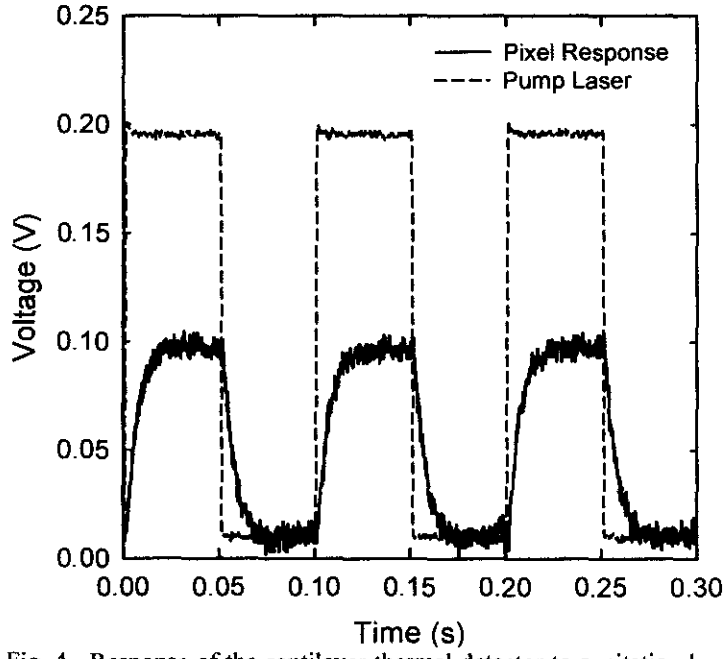

Fig. 4. Response of the cantilever thermal detector to excitation by a pulse diode laser driven by a square-wave signal. The frequency of the excitatio signal was 10 Hz. The data yielded the response time of 6 ms.

features, although with different relative intensities; a large, broadband response is also noted at low frequencies.

Finite element analysis and analytical calculations, with material properties from Table 1, yielded $\Delta z/\Delta T$ of 76 nm/K and 78 nm/K, respectively. Our experimental measurements yielded $\Delta z / \Delta T$ of about 50 nm/K. The difference in these values can be explained by margins in determining the structural parameters and material properties of the fabricated detectors as well as by inaccuracies in local temperature measurements.

Table 1. Material properties for the materials in the FPAs

Material	**Density** ρ (Kg/m^3)	**Young's modulus** E (GPa)	**Coefficient of Thermal Expansion, CTE** (10^{-6} K^{-1})	**Poisson's ratio,** ν	**Thermal conductivity,** g (W m^{-1} K^{-1})	**Heat Capacity,** c (J/kg K)
Silicon Nitride	2400	180	0.8	0.2	19	691
Gold	19300	77	14.2	0.42	296	129

During regular operation of the cantilever thermal detector in the evacuated chamber at a pressure of 10 mTorr, the main heat loss mechanism is determined by conductance through two beams ("legs") connecting the suspended bimaterial region of the device to the substrate. Thermal conductance G is calculated as $G=2gA/l$ where g is the thermal conductivity of the

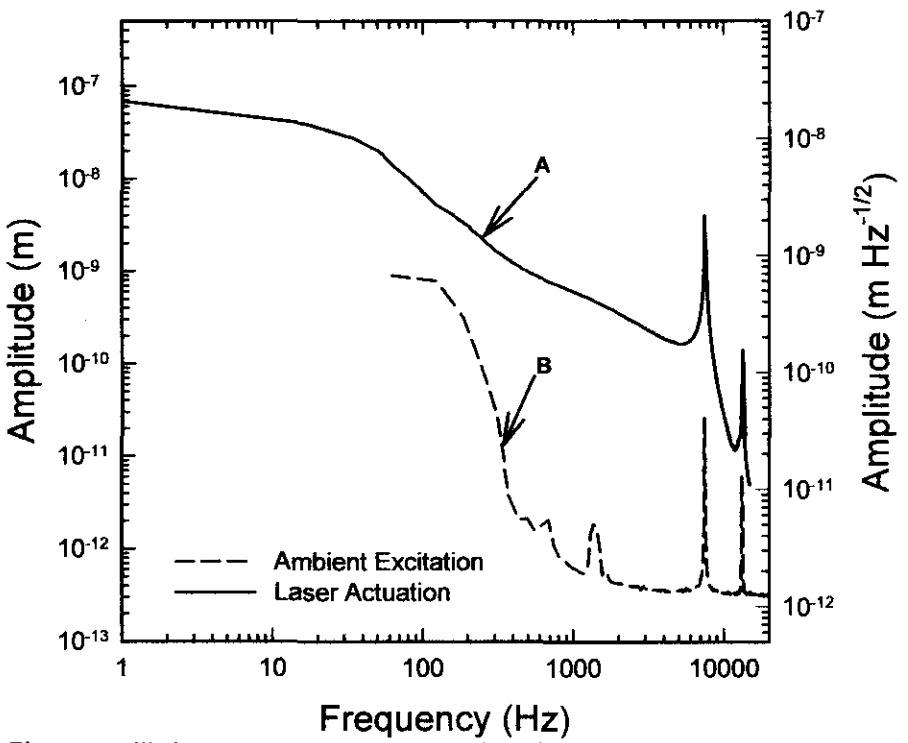

Fig. 5. Oscillation spectrum of the MEMS pixels in the frequency range of 0 to 15 kHz. The two peaks at 7.4 kHz and 12 kHz represent fundamental transverse resonance modes of the head and legs, respectively.

material (Table 1), A is the cross-sectional area, and l is the length of the heat path. Factor of 2 comes from the fact that the pixel head is connected to the substrate via two legs. For the current geometry, G is calculated to be 3.12×10^{-7} W/K. A response time for these structures calculated as $\tau = C/G$, where C is the heat capacity of the detector and G is determined by conductance through the legs only, is 14 ms. Experimental measurements of the response time were performed using the photothermal excitation with a laser driven by a square wave signal. The pumping laser response and the pixel response are displayed in Figure 5. Frequency of the square signal was 10Hz and its amplitude was 30mV. After performing the exponential fit to both rising and decaying segments, the response time of 6 ms was obtained. Using this value of the response time, the thermal conductance G was calculated to be 6.47×10^{-7} W/K. The difference between the values of thermal conductance calculated using experimentally measured response time and materials properties is related to the fact that the conduction through the legs is not the only heat dissipation pathway under the actual experimental conditions. In particular, radiative heat exchange may have contributed significantly when the temperature of the pixel increased due to absorbed energy from the pumping and readout lasers. Assuming that the pixel with an emissivity of unity was at 400 K, we obtained $G_{rad} = 9.73 \times 10^{-8}$ W/K. Thus, this value of thermal conductance yields the response time of 10 ms.

Background fluctuation limited and temperature fluctuations limited noise equivalent temperature differences $NETD_{BF}$, $NETD_{TF}$ and $NETD_{TM}$ were calculated using the following relationships[6]:

$$NETD_{BF} = \frac{8F^2\left[2k_B\sigma B\left(T_D^5 + T_B^5\right)\right]^{1/2}}{t_0(\eta A)^{1/2}(\Delta P/\Delta T)_{\lambda_1-\lambda_2}} \tag{1}$$

$$NETD_{TF} = \frac{8F^2 T_D\left(k_B BG\right)^{1/2}}{t_0\eta A(\Delta P/\Delta T)_{\lambda_1-\lambda_2}} \tag{2}$$

$$NETD_{TM} = \frac{8F^2}{t_0\eta A(\Delta P/\Delta T)_{\lambda_1-\lambda_2}}\frac{1}{R}\left(\frac{k_B T_D B}{kQ\omega}\right)^{1/2} \tag{3}$$

where F is the focal ratio of the optics, k_B is the Boltzmann constant (1.38×10^{-23} J/K), σ is the Stefan Boltzmann constant (5.67×10^{-8} J/K^{4}m^{2}s), B is the electrical bandwidth, T_D is the detector temperature, T_B is the background temperature, t_0 is the transmission coefficient of the optics, η is the absorptivity of the detector and $(\Delta P/\Delta T)_{\lambda 1-\lambda 2}$ is the change in power per unit area radiated by a blackbody at temperature T with respect to T measured within the spectral band from λ_1 to λ_2 and G is the total thermal conductance of the detector along the legs. Calculated $NETD_{BF}$, $NETD_{TF}$ and $NETD_{TM}$ were 2.52 mK, 14.2 mK and 150 mK respectively. The values used for calculations were F=1, B=30 Hz, T_D and T_B=307 K, t_0=0.5, η=0.5, A=3×10^{-9} m^2, $(\Delta P/\Delta T)_{8\text{-}14\mu m}$=2.62 W/m^{2}K, G=3.12×10^{-7} W/K, R=0.16 m/W (calculated using $\Delta z/\Delta T$), k=0.024 N/m, Q=6000, along with the material properties from Table 1. The total calculated $NETD$ was calculated to be 151 mK.

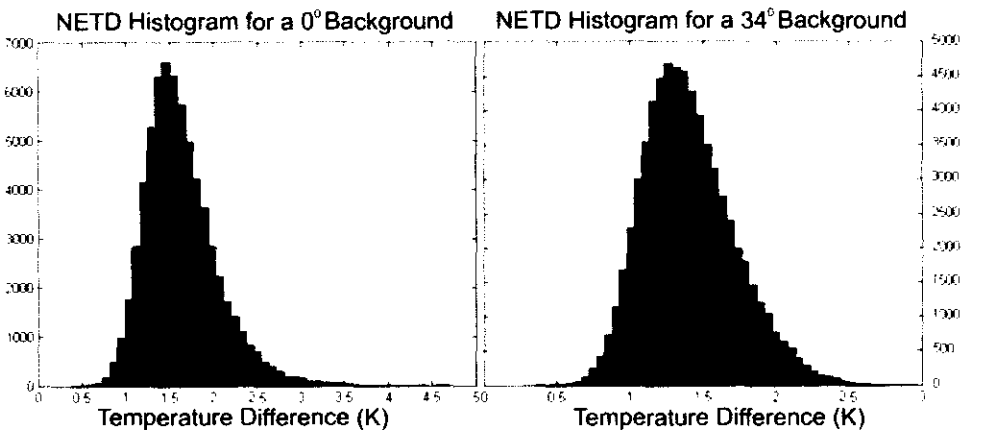

Fig. 6. *NETD* histograms obtained for two different target temperatures show that majority of the pixels have a *NETD* of about 1.5 K.

Fig. 7. An example of an image of a human obtained using the implemented MEMS IR system.

The value of *NETD* was also obtained by analyzing the experimentally acquired images of a full frame blackbody target maintained at different temperatures. For each pixel in the FPA responding to the blackbody, a value of *NETD* was calculated using[7]:

$$NETD = \frac{C_N}{C_s}(T_s - T_B) \tag{4}$$

where C_s is the averaged output level of the CCD camera pixel, and C_N represents the value for the noise. T_s and T_B are the temperatures of the source (target) and the background, respectively. The *NETD* histograms obtained for the MEMS IR imager at target temperatures of 273 K and 307 K are shown in Figure 6. The histograms have peaks at about 1.5 and 1.3 K for 273 K and 307 K, respectively. Some pixels, however, exhibited *NETD* values as low as 486 mK.

In order to test the IR imaging system, a uniform cold object was first positioned in front of the IR lens. The snapshot of the FPA was then taken by the CCD and stored. After replacing the cold object with a target to be imaged, images of the FPA were continuously acquired in a video mode with a frequency of 30 fps. During the image acquisition the background image was subtracted from each frame and the result of this subtraction was displayed in real time.

An example of images, obtained using the implemented system is shown in Figure 7. The pixels that appear darker indicate that a certain fraction of the pixels were deflected at angles different from the rest of the FPA. Hence, the portion of the readout beam reflected off them was blocked by the aperture and was missing in the output image.

4.3. References

1 R. Amantea, L.A. Goodman, F. Pantuso et al. (1998) in Infrared Technology and Applications XXIV, eds. Andresen, B. F. & Scholl, M. S. Proc. SPIE, Vol. 3436, pp. 647.

2 T. Perazzo, M. Mao, O. Kwon et al., "Infrared Vision Using Uncooled Micro-Optomechanical Camera," *Applied Physics Letters.* 74(23), 3567-3569 (1999).

3 J. Varesi, J. Lai, T. Perazzo et al., "Photothermal Measurements at PicoWatt Resolution Using Uncooled Micro-Optomechanical Sensors," *Applied Physics Letters.* 71(3), 306-308 (1997).

4 Y. Zhao, M. Y. Mao, R. Horowitz et al., "Optomechanical uncooled infrared imaging system: Design, microfabrication, and performance," *Journal of Microelectromechanical Systems.* 11(2), 136-146 (2002).

5 P.G. Datskos and N.V. Lavrik, in *Encyclopedia of Optical Engineering*, edited by Ronald Driggers (Dekker, New York, 2003), Vol. 1, pp. 349 - 357.

6 P. G. Datskos, N. V. Lavrik, and S. Rajic, "Performance of uncooled microcantilever thermal detectors," *Review of Scientific Instruments.* 75 (4), 1134-1148 (2004).

7 Paul W. Kruse, "A Comparison of the Limits to the Performance of Thermal and Photon Detector Imaging Arrays," *Infrared Physics and Technology* 36, 869 (1995).

8 T.W. Kenny, J.K. Reynolds, J.A. Podosek et al., "Micromachined Infrared Sensors Using Tunneling Displacement Transducers," *Review of Scientific Instruments.* 67 (1), 112 (1996).

9 N. V. Lavrik and P. G. Datskos, "Femtogram mass detection using photothermally actuated nanomechanical resonators," *Applied Physics Letters.* 82(16), 2697-2699 (2003).